The role of low energy resonances in the stereodynamics of cold He+D_2 collisions

Pablo G. Jambrina,[†] Masato Morita,[‡] James F. E. Croft,[¶] F. Javier Aoiz,[‖] and Naduvalath Balakrishnan[*,‡]

†*Departamento de Química Física, University of Salamanca, Salamanca 37008, Spain. e-mail: pjambrina@usal.es*

‡ *Department of Chemistry and Biochemistry, University of Nevada, Las Vegas, Nevada 89154, USA*

¶*Department of Physics, University of Otago, Dunedin 9054, New Zealand. e-mail: j.croft@otago.ac.nz*

§*Dodd-Walls Centre for Photonic and Quantum Technologies, Dunedin 9054, New Zealand.*

‖*Departamento de Química Física, Universidad Complutense, Madrid 28040, Spain. e-mail:aoiz@quim.ucm.es*

E-mail: naduvala@unlv.nevada.edu

Abstract

In recent experiments using the Stark-induced Adiabatic Raman Passage technique, Zhou et al. measured the product's angular distribution for the collisions between He and aligned D_2 molecules at cold collision energies. The signatures of the angular distributions were attributed to a ℓ=2 resonance that governs scattering at low energies. A first principles quantum mechanical treatment of this problem is presented here using a highly accurate interaction potential for the He-H_2 system. Our results predict a very intense ℓ=1 resonance at low energies, leading to angular distributions that differ from those measured in the experiment. A good agreement with the experiment is achieved only when the ℓ=1 resonance is artificially removed, for example, by excluding the lowest energies present in the experimental velocity distribution. Our analysis revealed that neither the position nor the intensity of the ℓ=1 resonance significantly changes when the interaction potential is modified within its predicted uncertainties. Energy-resolved measurements may help to resolve the discrepancy.

Graphical TOC Entry

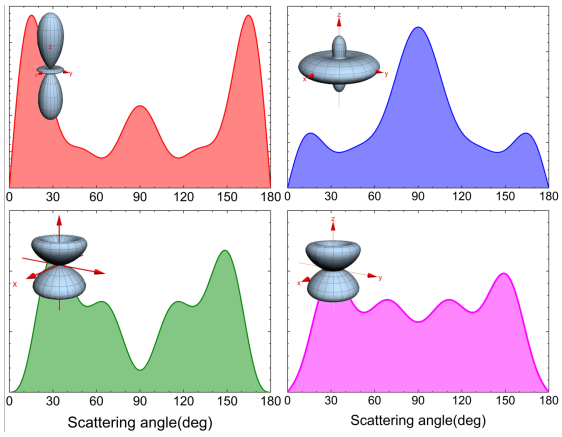

In molecular scattering, initial collision conditions that aid the system to reach the transition state geometries lead to higher reaction yields, while conditions that impede the system to reach such geometry lead to lower yields. This statement is usually related to the control of chemical reactions but it can be generalized to inelastic collisions.

Experiments that study the outcome of a molecular collision depending on the initial conditions have flourished in the last 10 years (see for example Refs. 1–13,13–19). Besides their importance for elucidating collision mechanisms, these experiments constitute a particularly effective probe of ab initio electronic-structure calculations and scattering methods. For inelastic collisions of NO($A^2\Sigma$) with He, Chandler, Costen, and coworkers determined how the orientation of the product's angular momentum ($\boldsymbol{j'}$) depends on the initial orientation of the NO molecule.[10] In Brouard's group, differences in the differential cross sections (DCS) for collisions between Rare Gases (Rg) and NO($X^2\Pi$) molecules were observed depending on the NO orientation: whether the collision was head-on or side-on and whether the Rg hits the molecule close to the O or N atom.[15–17] Zare and coworkers exploited the combination of co-propagating molecular beams with the Stark-induced adiabatic Raman Passage (SARP) method for state-preparation and alignment of the molecules.[11–13,18–20] In these experiments, the colliding molecules are co-propagated in the same molecular beam allowing relative collision energies near 1 K although the molecular velocities in the laboratory frame are much higher (about 2000 m/s). This is a particularly interesting regime which, when combined with the SARP method, allows for the study of sterodynamical preferences where only a few partial waves contribute. As such this combination is a powerful tool to probe the interaction potential.[11]

On the computational side, scattering calculations have been carried out to study how the outcome of bimolecular collisions depends on the initial collision conditions at low energies. In particular, since it has been experimentally determined that at cold energies the excitation function (cross section as a function of the collision energy) is governed by the presence of sharp resonance peaks,[21,22] a lot of effort has been devoted to establish to what extent resonance peaks can be controlled by selective experimental preparations.[23–28]

Recently, Zhou et al. presented a scattering experiment analogous to the double-slit experiment involving He+$D_2(v=2, j=2) \rightarrow$ He+$D_2(v'=2, j'=0)$ inelastic collisions near 1 K that yielded an interference term arising from two simultaneous bond-axis alignments of the D_2 molecule at $\pm$ 45° relative to the SARP laser polarization.[13,18] The DCSs for the inelastically scattered D_2 were found to be markedly different from a uni-axial preparation at 45° (or 135°) that does not include an interference term. In this Letter, we provide a first principles analysis of the experimental results of Zhou et al. using a highly accurate interaction potential for the He-H_2 system[29] that was benchmarked against high-resolution cavity measurements of line-shape parameters of H_2 perturbed by helium[30] and rotational Raman spectrum of D_2 in He.[31] Our quantum calculations reveal that scattering is governed by an ℓ=1 resonance at collision energies between 1 mK and 1 K. Striking differences between computed and experimental DCSs are observed, and calculations can only reproduce the experimental results if the ℓ=1 resonance is removed, which can be artificially done by excluding the low energies from our calculations. We find that the theoretical results are largely insensitive to the choice of quantum scattering method used and to modifications of the He–D_2 interaction potential within the uncertainties of the ab initio electronic structure calculations. Our results indicate the need for energy resolved measurements to resolve the discrepancy between theory and experiment for this benchmark system which may be accomplished using merged beam techniques.

Time independent quantum mechanical calculations were carried out using the coupled-channel (CC) formalism [32–35] as implemented in the MOLSCAT code.[36] Similar results were obtained using the ABC quantum scattering code[37] that uses the CC method in hyperspherical coordinates. The CC equations are constructed with a basis set that includes vibrational levels $v = 0-3$ and rotational levels $j = 0-2$ for $v = 3$, $j = 0-8$ for $v = 2$, $j = 0-12$ for $v = 1$, and $j = 0-18$ for $v = 0$. The CC equations are propagated from an atom-molecule separation of $R_{\rm min} = 2.0\ a_0$ to $R_{\rm max} = 50-100\ a_0$ (depending on the collision energy) using a log-derivative propagation method of Johnson.[38] A total of 290 energy values in a logarithmic scale in the range $10^{-6} - 20$ cm^{-1} relative to the initial $v = 2, j = 2$ level of D_2 are propagated to compute the

quenching cross sections. Total angular momentum quantum numbers $J = 0 - 9$ are included to secure convergence of the cross sections. Calculations were carried out on the BSP3 PES[29] for the He-H_2 system. Additional calculations on earlier versions of the BSP PES for the He-H_2 system[39] presented in the supplementary materials yielded similar results.

In He + D_2 SARP experiments,[13,18] a molecular beam of D_2 and He is co-expanded and collimated. Then, using SARP, nearly all the D_2 (v=0,j=0) is pumped into the excited D_2 (v=2,j=2) state. Changing the polarization direction of the pump and Stokes laser pulse with respect to the scattering frame (defined with z along the relative velocity of the colliding partners, $\boldsymbol{k}$, and the $x-z$ plane as that containing $\boldsymbol{k}$ and the recoil direction, $\boldsymbol{k'}$, after the collision) it is possible to produce anisotropic distributions of the D_2 internuclear axis. Following Ref. 40, $P(\theta_r, \phi_r)$, the probability density function (PDF) that describes the spatial distribution of the internuclear axis

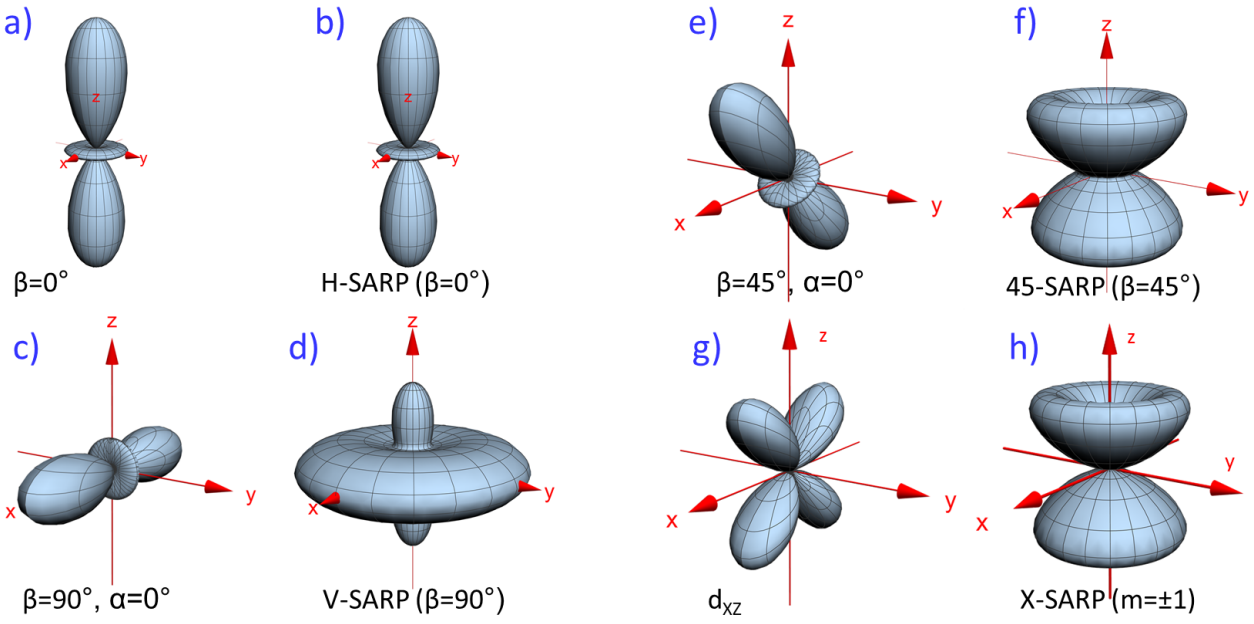

Figure 1: Stereodynamical portraits (i.e., PDFs for the internuclear axis distribution) for different experimental preparations. PDFs of the 1st and 3rd column depict the distributions for given values of β, and α, the angles that define the direction of the pump laser polarization in the scattering frame (panels a, c, e). The 2nd and 4th column display the alignment distributions integrated over α corresponding to the experimental PDF (panels b, d, f, and h). Note the similarities between 45-SARP, and X-SARP preparations upon integration over the azimuthal angle.

following SARP excitation is given by:

$$P(\theta_r,\phi_r)=\sum_{k=0}^{2j}\sum_{q=-k}^{q=k}\frac{2k+1}{4\pi}a_q^{(k)}\langle j0,k0|j0\rangle C_{kq}^{*}(\theta_r,\phi_r). \tag{1}$$

where θ_r, and ϕ_r are the polar and azimuthal angles that specify the direction of the D_2 internuclear axis with respect to the scattering frame, C_{kq} is the modified spherical harmonic, $\langle....|..\rangle$ is a Clebsch-Gordan coefficient, and $a_q^{(k)}$ are the extrinsic (preparation) polarization parameters in the $\boldsymbol{k}-\boldsymbol{k}'$ frame. In general terms, the initial state is prepared in the laboratory-fixed frame where Z is defined along the pump and Stokes polarization vector, assuming for the time being, parallel to each other. In this frame the polarization parameters are given by $A_0^{(k)}$ and are related to those in the scattering frame by[40]

$$a_q^{(k)}=A_0^{(k)}\left[D_{q0}^{k}(\alpha,\beta,\gamma=0)\right]^{*}=C_{kq}(\beta,\alpha)A_0^{(k)}, \tag{2}$$

where β and α are the polar and azimuthal angles that define the direction of the laser polarization vector (Z axis) in the $\boldsymbol{k}-\boldsymbol{k}'$ scattering frame. Note that because the distributions we are considering have cylindrical symmetry around Z, the only non-vanishing $A_Q^{(k)}$ moments have $Q=0$. If the prepared state is $|j\,0\rangle$ then $A_0^{(k)}=\langle j0,k0|j0\rangle$. Varying the direction of the laboratory axis, Z, with respect to the scattering frame amounts to changing the D_2 alignment in the scattering frame.[40]

Equation 2 is only valid if the pump and Stokes pulses are parallel to each other. This is the case of H-SARP ($\beta=0^\circ$), V-SARP ($\beta=90^\circ$), and the uniaxial 45° SARP preparation ($\beta=45^\circ$). The PDFs for H-SARP($\beta=0^\circ$), $\beta=90^\circ$, $\beta=45^\circ$, are shown in panels (a), (c), and (e) of Fig.1, where the α angle has been chosen as zero.

In Ref. 13, Zhou et al. also prepared the so-called biaxial state (X-SARP) using a cross-polarized pump (along Z) and Stokes (along X) pulses that allow to prepare a pure state as a superposition of $|j=2,m=\pm1\rangle$. For the X-SARP preparation, Eq. 2 is not valid, and the only

non-zero $A_Q^{(k)}$ moments are given by (see SI for derivation):

$$A_0^{(0)} = 1 \qquad A_0^{(2)} = -\frac{1}{\sqrt{14}} \qquad A_2^{(2)} = A_{-2}^{(2)} = -\frac{1}{2}\sqrt{\frac{3}{7}} \tag{3}$$
$$A_0^{(4)} = -\frac{2}{3}\sqrt{\frac{2}{7}} \qquad A_2^{(4)} = A_{-2}^{(4)} = \frac{1}{3}\sqrt{\frac{5}{7}},$$

that lead to the same PDF, $|d_{XZ}|^2$, as for a d_{XZ} spherical harmonic in the lab frame (X, Y, Z) now defined by the directions of the pump and Stokes laser polarizations. In the general case, to obtain the polarization parameters in the scattering frame, it would be necessary to use the expression

$$a_q^{(k)} = \sum_Q [D_{qQ}^k(\alpha,\beta,\gamma)]^* A_Q^{(k)}. \tag{4}$$

However, if the Z axis is made to coincide with the z axis ($\equiv \boldsymbol{k}$) of the scattering frame (which in the experiment is the direction of the flight axis), β=0, and the angle γ can be taken arbitrarily to be zero, yielding

$$a_q^{(k)} = \sum_Q [D_{qQ}^k(\alpha,0,0)]^* A_Q^{(k)} = \sum_Q e^{iq\alpha}\, d_{qQ}^k(0) = A_q^{(k)}\, e^{iq\alpha}, \tag{5}$$

where $d_{qQ}^k(0) = \delta_{qQ}$ is the reduced rotation matrix for $\beta = 0$. Therefore, $a_q^{(k)}$ and $A_q^{(k)}$ differ only by a phase factor (the azimuthal angle α) and Eq. (1) for the X-SARP preparation can be written as

$$P(\theta_r,\phi) = \sum_{k=0}^{2j} \sum_{q=-k}^{q=k} \frac{2k+1}{4\pi} A_q^{(k)} \langle j0,k0|j0\rangle C_{k,q}^*(\theta_r,\phi), \tag{6}$$

where the azimuthal angle is now $\phi = \phi_r - \alpha$, and the effect of changing α is the rotation around Z. The distribution of internuclear axis in the X-SARP case is portrayed in panel (g) of Fig. 1.

In the experiments using SARP preparation[13,18] the collision partners were co-expanded in a single supersonic beam in an axially symmetric arrangement. Therefore, to properly reproduce the experimental internuclear axis distribution that corresponds to each of the measured DCS, integration should be carried out over the azimuthal angle, leading to the PDFs shown in panels

(b), (d), (f), and (h) of Fig. 1. The integrated PDFs are, of course, independent of the azimuthal angle.

The expression to obtain the observable DCS, i.e., the DCS for a given internuclear axis preparation, is[40]

$$\mathrm{d}\sigma(\theta|\beta,\alpha) = \sum_{k=0}^{2j} \sum_{q=-k}^{k} (2k+1) U_q^{(k)}(\theta) a_q^{(k)}, \tag{7}$$

where the spherical tensors of rank k, $U_q^{(k)}(\theta)$ are the j-polarization dependent differential cross sections, j-PDDCSs, which in terms of the scattering amplitudes can be written as:

$$U_q^{(k)}(\theta) = \frac{1}{2j+1} \sum_{m',m} f_{j'm',\,jm}(\theta)\, f^*_{j'm',\,jm+q}(\theta)\, \langle jm, kq | jm+q \rangle\,, \tag{8}$$

where $f_{j'm',\,jm}(\theta)$ is the scattering amplitude (where the indices that denote the initial and final vibrational states have been omitted for the sake of clarity). The expressions to compute $f_{j'm',\,jm}(\theta)$ from the Scattering matrix are given in the Supplementary Material. If the initial prepared state in the laboratory frame is $|j\ m=0\rangle$, *i.e.*, where the Stokes and pump pulses are parallel to each other such as in H-SARP, V-SARP, and 45-SARP, Eq. (7) can be written as:[28]

$$\mathrm{d}\sigma(\theta|\beta,\alpha) = \sum_{m'} \left| \sum_{m} C_{jm}(\beta,\alpha)\, f_{j'm',\,jm}(\theta) \right|^2. \tag{9}$$

For the particular case of a j=2 $\rightarrow$ j'=0 transition, Eq. (9) reduces to

$$d\sigma(\theta|\beta,\alpha) = \left| \frac{1}{2}(3\cos^2\beta - 1) F_{0,0} - \left[\sqrt{6}\sin\beta\cos\beta\cos\alpha\right] F_{0,1} + \left[\sqrt{\frac{3}{2}}\sin^2\beta\cos 2\alpha\right] F_{0,2} \right|^2 \tag{10}$$

where we have used a shorthand notation for the scattering amplitudes $f_{j'm',\,jm}(\theta) \equiv F_{m',m}$, and the symmetry relationship: $F_{0,m} = (-1)^m F_{0,-m}$.

Upon integration over the azimuthal angle, all moments with $q \neq 0$ vanish, and the observable

DCS is given by:

$$I_\beta(\theta) = d\sigma(\theta|\beta)/d\theta = \sin\theta \int_0^{2\pi} d\sigma(\theta|\beta,\alpha)\,\mathrm{d}\alpha = \pi \sin\theta \left[\frac{1}{2}(3\cos^2\beta - 1)^2 \left|F_{0,0}\right|^2 + 6\sin^2\beta\cos^2\beta \left|F_{0,1}\right|^2 + \frac{3}{2}\sin^4\beta \left|F_{0,2}\right|^2\right]. \tag{11}$$

Thus, the final expression for the different observable DCSs $I_\beta(\theta)$ are:

$$I_{\beta=0}(\theta) = I_H(\theta) = 2\pi\sin\theta \left|F_{0,0}\right|^2 \tag{12}$$

$$I_{\beta=90^\circ}(\theta) = I_V(\theta) = \pi\sin\theta \left[\frac{1}{2}\left|F_{0,0}\right|^2 + \frac{3}{2}\left|F_{0,2}\right|^2\right] = \frac{1}{4}I_H(\theta) + \frac{3}{2}\pi\sin\theta \left|F_{0,2}\right|^2 \tag{13}$$

$$I_{\beta=45^\circ/135^\circ}(\theta) = I_{+/-}(\theta) = \pi\sin\theta \left[\frac{1}{8}\left|F_{0,0}\right|^2 + \frac{3}{2}\left|F_{0,1}\right|^2 + \frac{3}{8}\left|F_{0,2}\right|^2\right]. \tag{14}$$

For the cross-polarized X-SARP experiment, Eq. 9 is not valid, and after integration over the azimuthal angle, Eq. (7) simplifies to (see SI for further details):

$$I_X(\theta) \;=\; 2\pi\sin\theta \left|F_{0,1}\right|^2. \tag{15}$$

There are four characteristics of the observable DCS that we wish to draw our attention to:

- The observable DCS shows coherences between states with different m. These coherences disappear upon integration in the azimuthal angle (*i.e.*, terms associated with $q \neq 0$ vanish), making possible to compute the observable DCS as the weighted sum of the DCS for pure m states.

- $I_+(\theta)$ can be obtained as a combination of $I_V(\theta)$ and $I_X(\theta)$ as follows:

$$I_+(\theta) = \frac{3}{4}I_X(\theta) + \frac{1}{4}I_V(\theta). \tag{16}$$

- Assuming that the experiment integrates over the azimuthal angle, it is not possible to isolate

the contribution from $m = \pm 1$ without a cross-polarized experiment. If integration over azimuthal angle is not carried out, it could be possible to isolate $m = \pm 1$ by setting β=54.7° (magic angle), and α = 45° (or 135°).

- As stated in Ref. 18, and explained in the SI, it is possible to decompose the wave-function associated to X-SARP ($|\psi_X\rangle$) as a superposition of any pair of $|\psi_\beta\rangle$ and $|\psi_{\pi-\beta}\rangle$ states ($0 < \beta < 90$). In the particular case of β=45° the resulting expression is:

$$I_X(\theta) = \frac{2}{3} I_+(\theta) + \frac{1}{3} I_{\rm int}(\theta)\,, \tag{17}$$

where the interference term is given by

$$I_{\rm int}(\theta) = -\sin\theta \left[\frac{\pi}{4} \left|F_{0,0}\right|^2 - 3\pi \left|F_{0,1}\right|^2 + \frac{3\pi}{4} \left|F_{0,2}\right|^2 \right]. \tag{18}$$

Before presenting the DCSs for the different experimental internuclear axis distributions, we shall first present the unpolarized integral cross section (ICS) for the inelastic collisions between He + D_2 in the collision energy ($E_{\rm coll}$) range relevant to the experiment. The left panel of Fig. 2 shows the excitation functions (ICS as a function of $E_{\rm coll}$) in the $10^{-6} - 20$ K range. In agreement with previous calculations from Zhou and Chen[41] for He + D_2 (v=0,j=2) $\rightarrow$ He + D_2 (v=0,j=0) collisions on the BSP PES,[39] the excitation function exhibits two salient features: i) a dominant resonance peak at around 0.02 K that results in a 30-fold increase of the cross section, and ii) a small bump around 1.6 K. Partial wave resolution of the excitation function allows us to assign the small bump around 1.6 K to the opening of ℓ=2 partial-wave, and the 0.02 K resonance peak to a ℓ=1 resonance. Moreover, the ℓ=1 resonance peak is composed of two peaks corresponding to J=1 (ℓ'=1) and J=3 (ℓ'=3). A similar resonance profile was observed for other systems.[42] Except for those features, the excitation functions at the lowest energies (dominated by ℓ=0, s-wave scattering) is proportional to $E_{\rm coll}^{-1/2}$, as expected in the Wigner threshold regime.[43,44]

Previous studies of inelastic collisions at cold energies have shown that the intensity of the

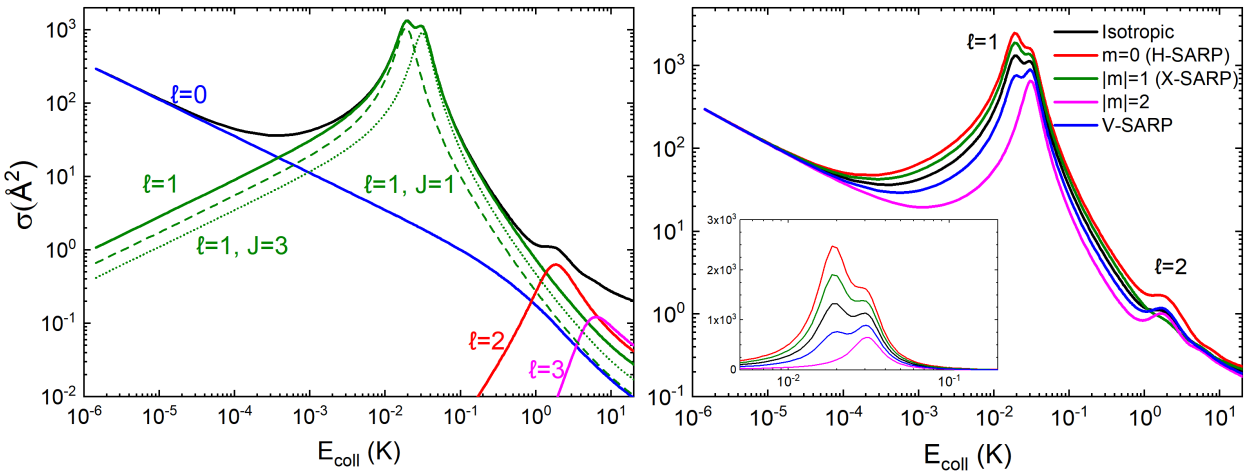

Figure 2: Left panel: Partial-wave-resolved excitation functions for He+$D_2(v=2, j=2 \rightarrow v'=2, j'=0)$ collisions. Right panel: Excitation functions for D_2 ($v=2, j=2 \rightarrow v'=2, j'=0$) by collisions with He for different initial preparations of the D_2 rotational state. The inset shows a zoom of the excitation function around the energy of the resonance in a linear scale.

resonance peak can be modulated by suitable alignments of the molecular bond axis.[25,27,28,42] To show how much control can be exerted on the ℓ=1 resonance by the initial preparations of internuclear axes, the right panel of Fig. 2 displays the excitation function for H-SARP (in which only m=0 contributes), X-SARP (where only $m = \pm 1$ contribute), and V-SARP (that includes contributions from m=0, and $\pm$ 2). These preparations have been depicted in Fig. 1. In addition, for the sake of comparison, the excitation function for m=2 is also shown. As was demonstrated in Ref. 45 there is no control over the ICS for ℓ =0 and, accordingly, in the Wigner regime all preparations converge to the value of the isotropic ICS.

For $E_{\rm coll} > 10^{-4}$ K, cross sections display sensitivity to different stereodynamic preparations, and at the resonance peak H-SARP yields larger cross sections than X-SARP and V-SARP. However, the resonance is prominent for the three preparations, and it is not possible to find a preparation for which the resonance disappears, as in the case for HD + H_2 inelastic collisions.[25] Nevertheless, it is possible to remove the contribution of (ℓ=1,J=1) peak, if a pure m=2 state could be prepared. In the case of the smaller ℓ =2 peak, it is the X-SARP (m=1) preparation that nearly washes out the observed peak. Overall, H-SARP preparation leads to larger cross sections at all energies including the ℓ=1 and ℓ=2 peaks, indicating that the collision mechanisms do not change

significantly with $E_{\rm coll}$, in particular at the resonance.

To elucidate the effect of different preparations on the DCS integrated over the azimuthal angle, Fig. 3 shows the differential cross sections at four different energies: 10^{-5}, 2×10^{-2}, 1.6, and 3 K, where $\mathrm{I}_\beta(\theta)$ are divided by $\sin\theta$ to highlight the strong preference for extreme forward and backward scattering (results where the $\sin\theta$ term is retained are shown in Fig. S1). At $E_{\rm coll}$ =10^{-5} K (well within the Wigner regime), no control can be achieved at the integral cross section level, but the DCS shows sensitivity to the different initial preparations.[45] For the H-SARP preparation (m=0) the DCS shows three salient peaks, at 0°, 90°, and 180°, whereas the isotropic (unpolarized) DCS is essentially independent of the scattering angle. The m=±2 component of V-SARP DCS (Eq. (13)) results in a Gaussian function centered at 90°, which when combined with the m=0 contribution, leads to a DCS with a prominent 90° peak. For X-SARP, only m=±1 contributes,

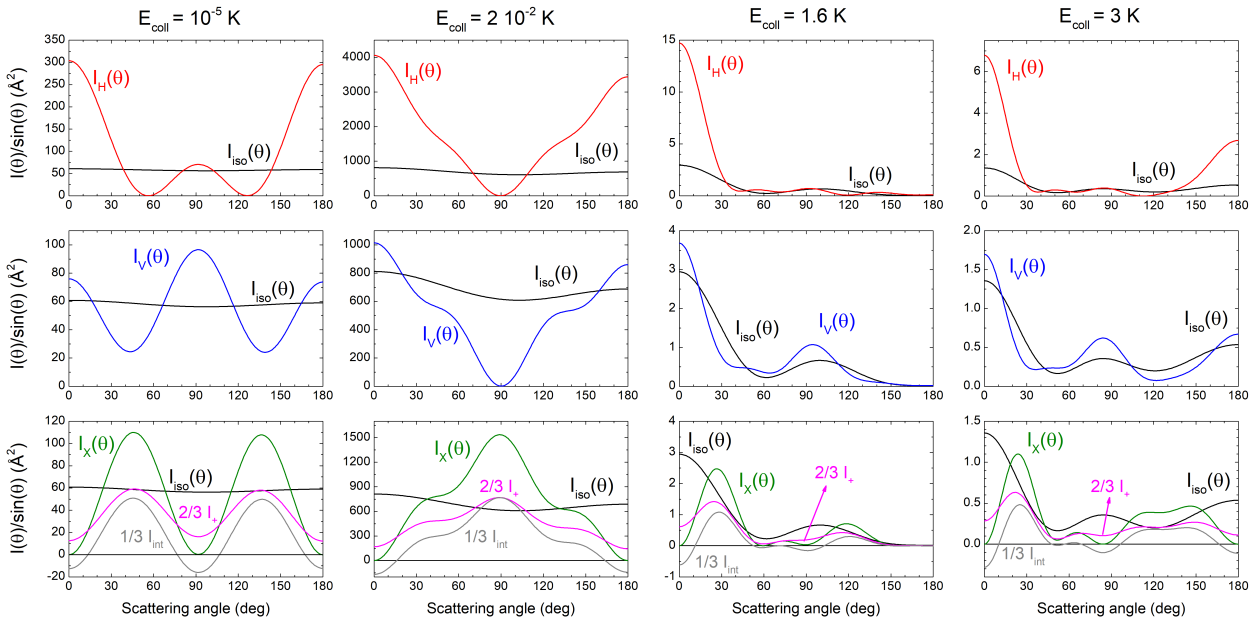

Figure 3: Differential Cross Sections for He+D_2 ($v=2, j=2 \rightarrow v'=2, j'=0$) collisions for different initial preparations of the D_2 rotational state at four different energies: 10^{-5}, 2×10^{-2}, 1.6, and 3 K. The top and middle panels show the results integrated over the azimuthal angle for H-SARP and V-SARP. The bottom panels show X-SARP along with 45-SARP (I_+) preparations, and $\mathrm{I_{int}}$, the interference term. In all panels the isotropic (unpolarized) DCS is shown for the sake of comparison. To see how the shape of the DCS evolves with $E_{\rm coll}$, in Fig. S3 the normalized DCS are shown as a function of $E_{\rm coll}$. The latter results clearly show how the shape of the DCS is governed by the ℓ=1 resonance.

and if only $\ell = 0$ is present, the DCS shows maxima at 45° and 135°, and nodes at 0°, 90°, and 180°. As a consequence of the connection between X-SARP, V-SARP, and 45-SARP DCSs (Eq. (16)-(17)), the latter displays a more isotropic DCS.

As shown in Fig. 2, at 2×10^{-2} K the scattering is dominated by the ℓ=1 partial wave. If only ℓ=1 contributes, the DCS should feature a node at 90° for m=0, 2, and it would be forward-backward symmetric. The tiny contribution of ℓ=0 slightly breaks the forward-backward symmetry of the DCS, with a non-zero value at 90° for m=0, 2. This minimum at 90° for H-SARP (only m=0) and V-SARP (m=0 and 2) is then a fingerprint of the ℓ=1 resonance. The fact that partial-waves that barely contribute to the ICS could modulate the DCS via interference is common, and in some cases it can even determine the shape of the DCS.[46,47] For DCS-X, there is only contribution from $|m|$=1 and, hence, we observe a maximum at 90°.

For $E_{\text{coll}} > 1$ K, ℓ=2 begins to contribute and we enter the multiple partial wave regime with the DCS no longer forward-backward symmetric (it is possible to obtain symmetric DCS for systems in which many partial-waves contribute, but an asymmetric DCS implies more than one partial-wave). At E_{coll} = 1.6 K, forward scattering is preferred, in particular for H-SARP that features a prominent forward peak. For DCS-V, m=2 also contributes, leading to a noteworthy maximum at 90°. For X-SARP the DCS is also predominantly forward, although no scattering occurs at 0°. At the highest energy shown, E_{coll} = 3.0 K, the only change is the larger contribution of backward scattering, displaying a backward peak for H-SARP and V-SARP DCSs.

As discussed earlier, the He + D_2 SARP experiments[13,18] were carried out using a single collimated molecular beam in which D_2 and He were co-expanded. Based on the experimental collision speeds, if the beam were perfectly collimated, the resulting collision energy distribution would be that shown in the top left panel of Fig. 4 (see also the supplementary materials of Ref. 13). If the small divergence of the beam (12 mrad=0.7°) is taken into account, the resulting 3D E_{coll}–distribution would be that shown in the lower left panel of Fig. 4. In the other panels, we present the observable DCSs for different initial preparations averaged over the corresponding collision energy distributions. Since experimentally it is not possible to distinguish between

scattering at θ and $\pi - \theta$, the DCSs shown here are symmetrized as discussed in the SARP experiments.[13,18] Apart from the irrelevant absolute value, there is no difference in the shape of the observable DCSs obtained for the 1D and 3D energy distribution functions. For both H-SARP and V-SARP the main feature is the deep minimum observed at θ=90°, with four maxima at 15 and 60, 120, and 165° of different intensities. For X-SARP and 45-SARP we observe three maxima, at 30, 90, and 150°.

Results presented in Fig. 4 are clearly at variance with the experimental results (reproduced as black dots in Fig. 5). These differences are especially noteworthy at θ=90°. At this angle, experimental results show maxima for H-SARP, and V-SARP and a deep minimum for X-SARP. Our results, instead show deep minima for V-SARP, and H-SARP and a maximum for X-SARP. The evolution of the shape of the DCS as a function of $E_{\rm coll}$ displayed in Fig. S3 clearly indicates that these features are caused solely by the ℓ=1 resonance. We can artificially remove ℓ=1 contribution, for example, excluding the averaging over $E_{\rm coll} < 1$ K. By doing this we obtain

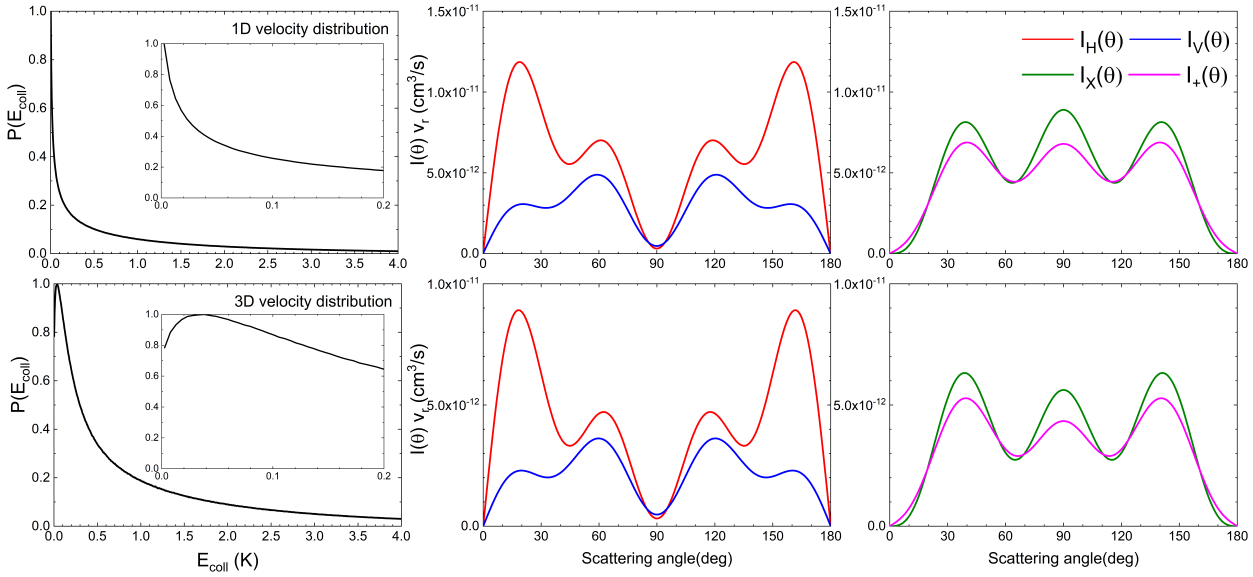

Figure 4: Velocity-averaged differential rate coefficients for D_2 ($v = 2, j = 2 \rightarrow v' = 2, j' = 0$) by collisions with He for the H-SARP, V-SARP, X-SARP, and 45-SARP preparations of the initial D_2 alignments as a function of the scattering angle. Results are shown for two different $E_{\rm coll}$ distributions, one assuming a 1D distribution (top panels), and another assuming a 3D distribution (bottom panels). The insets of the left panels display the maxima of the $E_{\rm coll}$ distributions, P($E_{\rm coll}$). Results assuming a 3D distribution with a larger divergence are shown in Fig. S2.

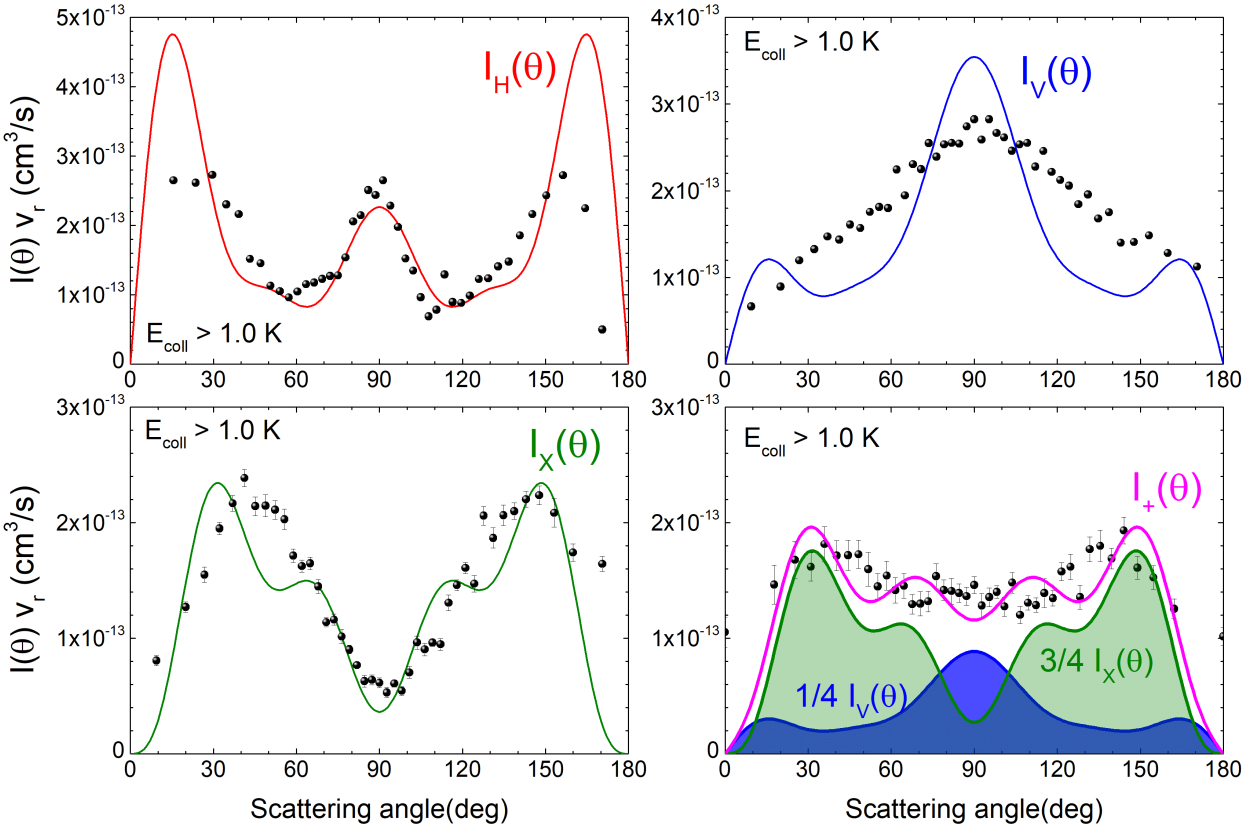

Figure 5: Velocity-averaged differential rate coefficients for D_2 ($v = 2, j = 2 \rightarrow v' = 2, j' = 0$) by collisions with He for the H-SARP, V-SARP, X-SARP, and 45-SARP preparations of the initial D_2 orientations as functions of the scattering angle. Results are shown assuming a 3D velocity distribution, and excluding $E_{\rm coll} < 1$ K. Experimental results from Ref. 13 and 18 are included as black dots. As shown in Eq. (16), $I_+(\theta)$ can be obtained adding 1/4 $I_V(\theta)$ and 3/4 $I_X(\theta)$, and these two contributions are also shown in the bottom right panel.

the results displayed in Fig. 5, which reproduce the experimental results fairly well, including the effect of the interference term in X-SARP.

Altogether, our results show that there is a clear discrepancy between calculations and experiment and that this discrepancy is caused by a strong $\ell = 1$ resonance whose overwhelming contribution breaks the agreement with the experimental data from Ref. 18. In Ref. 13, based on the centrifugal energy barriers the authors estimate that the differential rate coefficient (DCS multiplied by the relative velocity) would be roughly 10 times larger for ℓ=2 than for ℓ=1, which could somewhat explain why $\ell = 1$ resonance is not experimentally observed. In the bottom panel of Fig. S4 we show that, indeed, the incoming flux at the energies of ℓ=2 collisions is dominant. However, the contribution of ℓ=1 found in the present work is so prevailing that it dominates the contribution from lower collision energies (see panels a-c of Fig. S4).

The disagreement between theory and experiment for He + D_2 (v=2,j=2) inelastic collisions is unexpected. For Rg + NO($^2\Pi$) inelastic collisions, an excellent agreement between theory and experiment is obtained[22,48] even though calculations for the latter system involve more electrons and potential energy surfaces, and should be, in principle, less accurate.

To carry out our calculations we used the BSP3 PES, which is the best available potential energy surface for He+H_2 collisions and it is computed with a very large-basis set at the CCSD(T) level augmented by corrections for higher-order excitations (up to full configuration interaction level) and includes the diagonal Born-Oppenheimer correction. Thus, as far as electronic structure calculations are considered, there is a limited room for improvement. Moreover, the BSP3 PES has been shown to yield highly accurate results for Raman shifting and broadening cross sections for He-H_2 complexes in cavity experiments.[30]

One could argue that the position and intensity of a resonance could be sensitive to small changes of the interaction potential. To see if this is the case for this system, we examined the sensitivity of the ℓ=1 peak to the choice of the ab-initio potential used in the scattering calculations. To this end, we repeated our calculations using two additional PESs that were developed by Garberoglio et al.[49] based on the original BSP potential.[39] They are referred to as "BSP+" and

"BSP−" potentials which are fitted to (energy+uncertainty) and (energy-uncertainty) of the ab initio data, respectively. These "upper limit" and "lower limit" versions of the BSP potentials were earlier used to estimate uncertainties for the fully quantum calculations of the second virial coefficients to temperatures as low as 8 K for He-H_2 (16 K for He-D_2 due to limited experimental data) that yielded good agreement with experiments.[49] Using these potentials, the position of the ℓ=1 resonance peak changes, in particular with the BSP- potential (See Fig. S5), but the change is not enough to reduce the weight of ℓ=1 collisions after averaging over the experimental $P(E_{\rm coll})$, as shown in Fig. S6. We also explored the possibility of an error in the scattering calculations. To rule out this possibility, we repeated the calculations for different D_2 rovibrational states and also using the ABC code[37] which uses hyperspherical coordinates for the scattering calculations. Again, the ℓ=1 resonance peak is dominant (Fig S7 and S8).

To summarize, we have carried out quantum scattering calculations for the inelastic quenching of D_2 (v=2,j=2) in collisions with He atoms at cold energies. The excitation function is governed by a sharp peak at 0.02 K, due to a ℓ=1 resonance. We examined if the resonance peak could be modulated changing the relative direction of D_2 internuclear axis with respect to the approach direction. Although a considerable degree of control could be achieved, it is not possible to reduce the importance of the resonance significantly. The calculated differential cross sections for different internuclear axis distributions are clearly at variance with the experimental results of Ref. 13,18, unless the ℓ=1 resonance contribution is excluded from our calculations (by excluding contributions from $E_{\rm coll} < 1$ K). Indeed, we obtain near-quantitative agreement with the experiment when the ℓ=1 resonance contribution is excluded. The disagreement between theory and experiment is unexpected for this system due to the numerically exact nature of the quantum scattering calculations and the high-level ab-initio theory employed in the construction of the He-H_2 potential energy surface adopted in the calculations. Furthermore, ℓ=1 resonance is still dominant when the interaction potential is modified within its theoretical limits, and also if other vibrational states are sampled. Energy-resolved experiments and/or calculations are needed to discern the source of this discrepancy.

Supplementary material

See the supplementary material associated with this article for expressions for the scattering amplitudes and DCS in the orbital angular momentum representation, additional figures, and derivation of the polarization parameters and DCS associated to X-SARP.

Acknowledgement

We are grateful to Nandini Mukherjee providing us the experimental data in Ref. 13,18 and for helpful discussions. We thank Humberto da Silva Jr for useful comments. This work was supported in part by NSF grant No. PHY-2110227 (N.B.) and ARO MURI grant No. W911NF-19-1-0283 (N.B.). P.G.J. gratefully acknowledges grant PID2020-113147GA-I00 funded by MCIN/AEI/10.13039/, and F.J.A. acknowledges funding by the Spanish Ministry of Science and Innovation (Grant No. PGC2018-096444-B-I00).

Data availability statement

The data that support the findings of this study are available within the article and its supplementary material. Data is also available from the authors upon reasonable request.

References

(1) Wang, F.; Lin, J. S.; Liu, K. Steric Control of the Reaction of CH Stretch–Excited CHD_3 with Chlorine Atom. *Science* **2011**, *331*, 900–903.

(2) Wang, F.; Liu, K.; Rakitzis, T. P. Revealing the stereospecific chemistry of the reaction of Cl with aligned CHD_3 ($v1$= 1). *Nat. Chem.* **2012**, *4*, 636–641.

(3) Wang, F.; Liu, K. Differential steric effects in Cl reactions with aligned CHD_3 (v_1= 1) by the

R (0) and Q (1) transitions. I. Attacking the excited C–H bond. *J. Chem. Phys.* **2016**, *145*, 144305.

(4) Wang, F.; Liu, K. Differential steric effects in Cl reactions with aligned CHD_3 (v_1= 1) by the R (0) and Q (1) transitions. II. Abstracting the unexcited D-atoms. *J. Chem. Phys.* **2016**, *145*, 144306.

(5) Brouard, M.; Chadwick, H.; Gordon, S.; Hornung, B.; Nichols, B.; Aoiz, F. J.; Stolte, S. Rotational Orientation Effects in NO (X)+ Ar Inelastic Collisions. *J. Phys. Chem. A* **2015**, *119*, 12404–12416.

(6) Chadwick, H.; Nichols, B.; Gordon, S. D. S.; Hornung, B.; Squires, E.; Brouard, M.; Kłos, J.; Alexander, M. H.; Aoiz, F. J.; Stolte, S. Inelastic Scattering of NO by Kr: Rotational Polarization over a Rainbow. *J. Phys. Chem. Lett.* **2014**, *5*, 3296–3301.

(7) Brouard, M.; Chadwick, H.; Eyles, C. J.; Hornung, B.; Nichols, B.; Aoiz, F. J.; Jambrina, P. G.; Stolte, S. Rotational alignment effects in NO (X)+ Ar inelastic collisions: An experimental study. *J. Chem. Phys.* **2013**, *138*, 104310.

(8) Vogels, S. N.; Karman, T.; Klos, J.; Besemer, M.; Onvlee, J.; van der Avoird, J. O.; Groenenboom, G. C.; van de Meerakker, S. Y. T. Scattering resonances in bimolecular collisions between NO radicals and H_2 challenge the theoretical gold standard. *Nat. Chem.* **2018**, *10*, 435–440.

(9) Onvlee, J.; Gordon, S. D. S.; Vogels, S. N.; Auth, T.; Karman, T.; Nichols, B.; van der Avoird, A.; Groenenboom, G. C.; Brouard, M.; van de Meerakker, S. Y. T. Imaging quantum stereodynamics through Fraunhofer scattering of NO radicals with rare-gas atoms. *Nat. Chem.* **2017**, *9*, 226–233.

(10) Sharples, T. R.; Leng, J. G.; Luxford, T. F. M.; McKendrick, K. G.; Jambrina, P. G.; Aoiz, F. J.; Chandler, D. W.; Costen, M. L. Non-intuitive rotational reorientation in collisions

of NO(A $^2\Sigma^+$) with Ne from direct measurement of a four-vector correlation. *Nat. Chem.* **2018**, *10*, 1148–1153.

(11) Perreault, W. E.; Mukherjee, N.; Zare, R. N. Quantum control of molecular collisions at 1 kelvin. *Science* **2017**, *358*, 356–359.

(12) Perreault, W. E.; Mukherjee, N.; Zare, R. N. Cold quantum-controlled rotationally inelastic scattering of HD with H_2 and D_2 reveals collisional partner reorientation. *Nat. Chem.* **2018**, *10*, 561–567.

(13) Zhou, H.; Perreault, W. E.; Mukherjee, N.; Zare, R. N. Shape resonance determined from angular distribution in D_2 (v=2, j=2) + He $\rightarrow$ D_2 (v=2, j=0) + He cold scattering. *J. Chem. Phys* **2021**, *154*, 104309.

(14) Heid, C. G.; Walpole, V.; Brouard, M.; Jambrina, P. G.; Aoiz, F. J. Side-impact collisions of Ar with NO. *Nat. Chem.* **2019**, *11*, 662.

(15) Heid, C. G.; Bentham, I. P.; Walpole, V.; Jambrina, P. G.; Aoiz, F. J.; Brouard, M. Controlling the Spin-Orbit Branching Fraction in Molecular Collisions. *J. Phys. Chem. Lett.* **2021**, *12*, 310.

(16) Heid, C. G.; Bentham, I. P.; Walpole, V.; Gheorge, R.; Jambrina, P. G.; Aoiz, F. J.; Brouard, M. Probing the location of the unpaired electron in spin-orbit changing collisions of NO with Ar. *Phys. Chem. Chem. Phys.* **2020**, *22*, 22289.

(17) Walpole, V.; Heid, C. G.; Jambrina, P. G.; Aoiz, F. J.; Brouard, M. Steric Effects in the Inelastic Scattering of NO (X)+ Ar: Side-on Orientation. *J. Phys. Chem. A* **2019**, *123*, 8787.

(18) Zhou, H.; Perreault, W. E.; Mukherjee, N.; Zare, R. N. Quantum mechanical double slit for molecular scattering. *Science* **2021**, *374*, 960–964.

(19) Perreault, W. E.; Mukherjee, N.; Zare, R. N. HD ($v = 1$, $j = 2$, m) orientation controls HD-He rotationally inelastic scattering near 1 K. *J. Chem. Phys.* **2019**, *150*, 174301.

(20) Perreault, W. E.; Zhou, H.; Mukherjee, N.; Zare, R. N. A Bi-Axial Quantum State That Controls Molecular Collisions Like a Double-Slit Interferometer. *Frontiers in Physics* **2021**, *9*.

(21) Vogels, S. N.; Onvlee, J.; Chefdeville, S.; van der Avoird, A.; Groenenboom, G. C.; van de Meerakker, S. Y. T. Imaging resonances in low-energy NO-He inelastic collisions. *Science* **2015**, *350*, 787–790.

(22) de Jongh, T.; Besemer, M.; Shuai, Q.; Karman, T.; van der Avoird, A.; Groenenboom, G. C.; van de Meerakker, S. Y. T. Imaging the onset of the resonance regime in low-energy NO-He collisions. *Science* **2020**, *368*, 626–630.

(23) Croft, J. F. E.; Balakrishnan, N.; Huang, M.; Guo, H. Unraveling the Stereodynamics of Cold Controlled HD-H_2 Collisions. *Phys. Rev. Lett.* **2018**, *121*, 113401.

(24) Croft, J. F. E.; Balakrishnan, N. Controlling rotational quenching rates in cold molecular collisions. *J. Chem. Phys.* **2019**, *150*, 164302.

(25) Jambrina, P. G.; Croft, J. F. E.; Guo, H.; Brouard, M.; Balakrishnan, N.; Aoiz, F. J. Stereodynamical Control of a Quantum Scattering Resonance in Cold Molecular Collisions. *Phys. Rev. Lett.* **2019**, *123*, 043401.

(26) Morita, M.; Balakrishnan, N. Stereodynamics of rotationally inelastic scattering in cold He+HD collisions. *J. Chem. Phys.* **2020**, *153*, 091101.

(27) Morita, M.; Yao, Q.; Xie, C.; Guo, H.; Balakrishnan, N. Stereodynamic control of overlapping resonances in cold molecular collisions. *Phys. Rev. Research* **2020**, *2*, 032018.

(28) Jambrina, P. G.; Croft, J. F. E.; Balakrishnan, N.; Aoiz, F. J. Stereodynamic control of cold rotationally inelastic CO + HD collisions. *Phys. Chem. Chem. Phys.* **2021**, *23*, 19364.

(29) Thibault, F.; Patkowski, K.; Żuchowski, P. S.; Jóźwiak, H.; Ciuryło, R.; Wcisło, P.

Rovibrational line-shape parameters for H_2 in He and new H_2-He potential energy surface. *J. Quant. Spectrosc. Radiat. Transf.* **2017**, *202*, 308.

(30) Słowiński, M.; Thibault, F.; Tan, Y.; Wang, J.; Liu, A.-W.; Hu, S.-M.; Kassi, S.; Campargue, A.; Konefał, M.; Jóźwiak, H. et al. H_2-He collisions: Ab initio theory meets cavity-enhanced spectra. *Phys. Rev. A* **2020**, *101*, 052705.

(31) Martínez, R.; Bermejo, D.; Thibault, F.; Wcisło, P. Testing the ab initio quantum-scattering calculations for the D2–He benchmark system with stimulated Raman spectroscopy. *J. Raman Spectrosc* **2018**, *49*, 1339–1349, cited By 20.

(32) Blatt, J. M.; Biedenharn, L. C. The Angular Distribution of Scattering and Reaction Cross Sections. *Rev. Mod. Phys.* **1952**, *24*, 258–272.

(33) Arthurs, A. M.; Dalgarno, A. The theory of scattering by a rigid rotator. *Proc. R. Soc. London A* **1960**, *256*, 540–551.

(34) Alexander, M. H.; Dagdigian, P. J.; DePristo, A. E. Quantum interpretation of fully state-selected rotationally inelastic collision experiments. *J. Chem. Phys.* **1977**, *66*, 59–66.

(35) Alexander, M. H. Close-coupling studies of the orientation dependence of rotationally inelastic collisions. *J. Chem. Phys.* **1977**, *67*, 2703–2712.

(36) Hutson, J. M.; Green, S. MOLSCAT v.14. Swindon: Engineering and Physical Sciences Research Council, 1994.

(37) Skouteris, D.; Castillo, J.; Manolopoulos, D. ABC: a quantum reactive scattering program. *Comp. Phys. Comm.* **2000**, *133*, 128–135.

(38) Manolopoulos, D. E. An improved log derivative method for inelastic scattering. *J. Chem. Phys.* **1986**, *85*, 6425–6429.

(39) Bakr, B. W.; Smith, D. G. A.; Patkowski, K. Highly accurate potential energy surface for the He-H_2 dimer. *J. Chem. Phys.* **2013**, *139*, 144305.

(40) Aldegunde, J.; de Miranda, M. P.; Haigh, J. M.; Kendrick, B. K.; Saez-Rabanos, V.; Aoiz, F. J. How reactans polarization can be used to change and unravel chemical reactivity. *J. Phys. Chem. A* **2005**, *109*, 6200–6217.

(41) Zhou, B.; Chen, M. Quantum rotational scattering of H_2 and its isotopologues with He. *Mol. Phys.* **2017**, *115*, 2442–2450.

(42) Jambrina, P. G.; González-Sánchez, L.; Lara, M.; Menéndez, M.; Aoiz, F. J. Unveiling shape resonances in H + HF collisions at cold energies. *Phys. Chem. Chem. Phys.* **2020**, *22*, 24943–24950.

(43) Balakrishnan, N.; Forrey, R.; Dalgarno, A. Threshold phenomena in ultracold atom–molecule collisions. *Chem. Phys. Lett.* **1997**, *280*, 1–4.

(44) Lara, M.; Jambrina, P. G.; Aoiz, F. J.; Launay, J.-M. Cold and ultracold dynamics of the barrierless $D^+ + H_2$ reaction: Quantum reactive calculations for $\sim R^{-4}$ long range interaction potential. *J. Chem. Phys.* **2015**, *143*, 204305.

(45) Aldegunde, J.; Alvariño, J. M.; de Miranda, M. P.; Sáez Rábanos, V.; Aoiz, F. J. Mechanism and control of the F+H2 reaction at low and ultralow collision energies. *J. Chem. Phys.* **2006**, *125*, 133104.

(46) Jambrina, P. G.; Herráez-Aguilar, D.; Aoiz, F. J.; Sneha, M.; Jankunas, J.; Zare, R. N. Quantum interference between $H + D_2$ quasiclassical reaction mechanisms. *Nat. Chem.* **2015**, *7*, 661.

(47) Jambrina, P. G.; Menéndez, M.; Aoiz, F. J. Angular momentum scattering angle quantum correlation: a generalized deflection function. *Chem. Sci.* **2018**, *9*, 4837.

(48) Amarasinghe, C.; Perera, C. A.; Li, H.; Zuo, J.; Besemer, M.; van der Avoird, A.; Groenenboom, G. C.; Guo, H.; Suits, A. G. Collision-induced spin-orbit relaxation of highly vibrationally excited NO near 1 K. *Nat. Sci. 2*, e20210074.

(49) Garberoglio, G.; Patkowski, K.; Harvey, A. H. Fully Quantum Cross Second Virial Coefficients for the Three-Dimensional He–H_2 Pair. *Int. J. Thermophys* **2014**, *35*, 1435–1449.